AGU PUBLICATIONS

JGR

Journal of Geophysical Research: Atmospheres

RESEARCH ARTICLE
10.1002/2013JD020784

Key Points:
- Temperature tides from 30 to 110 km are characterized with lidar and WAM at McMurdo
- A new finding is the fast growth of 24 and 12 h tidal amplitudes above 100 km
- Larger Kp indices correspond to larger tidal amplitudes and faster growth rates

Correspondence to:
X. Chu and W. Fong,
Xinzhao.Chu@colorado.edu;
Weichun.Fong@colorado.edu

Citation:
Fong, W., X. Lu, X. Chu, T. J. Fuller-Rowell, Z. Yu, B. R. Roberts, C. Chen, C. S. Gardner, and A. J. McDonald (2014), Winter temperature tides from 30 to 110 km at McMurdo (77.8°S, 166.7°E), Antarctica: Lidar observations and comparisons with WAM, *J. Geophys. Res. Atmos.*, *119*, 2846–2863, doi:10.1002/2013JD020784.

Received 22 AUG 2013
Accepted 21 FEB 2014
Accepted article online 24 FEB 2014
Published online 18 MAR 2014

Winter temperature tides from 30 to 110 km at McMurdo (77.8°S, 166.7°E), Antarctica: Lidar observations and comparisons with WAM

Weichun Fong[1,2], Xian Lu[1], Xinzhao Chu[1,2], Tim J. Fuller-Rowell[1,3], Zhibin Yu[1,2], Brendan R. Roberts[1,2], Cao Chen[1,2], Chester S. Gardner[4], and Adrian J. McDonald[5]

[1]Cooperative Institute for Research in Environmental Sciences, University of Colorado Boulder, Boulder, Colorado, USA, [2]Department of Aerospace Engineering Sciences, University of Colorado Boulder, Boulder, Colorado, USA, [3]Space Weather Prediction Center, NOAA, Boulder, Colorado, USA, [4]Department of Electrical and Computer Engineering, University of Illinois at Urbana–Champaign, Urbana, Illinois, USA, [5]Department of Physics and Astronomy, University of Canterbury, Christchurch, New Zealand

Abstract We provide the first characterization of diurnal and semidiurnal thermal tides in temperature from 30 to 110 km in the winter season (May through August) at McMurdo (77.8°S, 166.7°E), Antarctica. The observations were made with an Fe Boltzmann temperature lidar in 2011 and 2012. Over 330 h of winter data are compiled into a composite day of temperature perturbations that significantly reduce the incoherent wave effects while preserving the coherent tidal signatures. Both diurnal and semidiurnal tides have small amplitudes (less than 3 K) below 100 km with vertical wavelengths of ~29 and ~23 km, respectively. A new finding of this study is the fast growth of diurnal and semidiurnal tidal amplitudes above 100 km to at least 15 K near 110 km, exceeding that of the freely propagating tides originating from the lower atmosphere. Such fast growth exists for all *Kp* index cases and diurnal amplitude increases to 15–30 K at 110 km with larger *Kp* indices corresponding to larger tidal amplitudes and faster growth rates. The slopes of diurnal tidal phases become steeper above 100 km, and the tidal phases barely change with altitude from 100 to 106 km. The tidal growth behavior is reproduced in the Whole Atmosphere Model (WAM) with phases comparable to the observations but magnitudes significantly underestimated. WAM compares reasonably well with the observations below 100 km. The observed significant amplitude increases and phase structure changes suggest additional tidal sources near or above 100 km, which deserve future investigation.

1. Introduction

Atmospheric tides are global-scale oscillations in pressure, density, temperature, and wind fields for which the periods are harmonics of a solar day. They can be classified as migrating (Sun-synchronous) and nonmigrating (non-Sun-synchronous) tides according to their horizontal phase velocities, i.e., migrating tides follow the motion of the Sun. The driving forces of migrating tides are mainly periodic absorption of solar radiation in the atmosphere, and those for nonmigrating tides are mainly latent heat release in the tropical region [*Hagan and Forbes*, 2002; *Zhang et al*., 2010a, 2010b] and nonlinear interactions between planetary waves and migrating tides [*Angelats i Coll and Forbes*, 2002; *Hagan and Roble*, 2001; *Murphy et al*., 2009]. Tides can obtain large amplitudes in the middle and upper atmosphere, where they modulate ionospheric variability via the *E* region dynamo effect [*Forbes et al*., 2000; *Forbes et al*., 2008], enhance vertical atmosphere coupling [*Forbes et al*., 2000; *Immel et al*., 2006], and cause instabilities by inducing significant temperature gradients and wind shears [*Hecht et al*., 1997; *Liu et al*., 2004]. Tides affect the propagation of gravity waves (GWs) [*Walterscheid*, 1981; *Lu et al*., 2009] and modulate GW momentum fluxes [*Fritts and Vincent*, 1987; *Espy et al*., 2004; *Liu et al*., 2013]. Tides also impact the vertical transport of atmospheric constituents and thereby the total solar heating in the upper part of the middle atmosphere [*Smith et al*., 2003].

Numerous observations have been carried out to characterize tides in the tropical and subtropical regions. However, in the polar region, observations of temperature tides are rare due to the lack of suitable temperature measurements. For satellite measurements, only observations from precessing satellites have the local time coverage needed for tidal studies, such as the Microwave Limb Sounder (MLS) on the Upper

Atmosphere Research Satellite (UARS) and the Sounding of the Atmosphere using Broadband Emission Radiometry (SABER) on the Thermosphere Ionosphere Mesosphere Energetics and Dynamics (TIMED) satellite. Even so, they are constrained by the orbital geometry and have limited coverage for high latitudes. For instance, SABER can only cover latitudes from 52°S to 83°N during most of the wintertime in the Southern Hemisphere [*Russell et al*., 1999] and the MLS on UARS only covers from 34°S to 80°N in May and July [*Forbes and Wu*, 2006]. There have been several studies of wind tides in the Antarctic region using ground-based radar observations, and particularly nonmigrating semidiurnal tide with wave number 1 has been extensively studied [*Forbes et al*., 1995; *Portnyagin et al*., 1998; *Baumgaertner et al*., 2005, 2006; *Murphy et al*., 2003, 2006, 2009; *Hibbins et al*., 2010]. Unfortunately, there is no simple relationship between tides in winds and those in temperatures since the latitudinal structures of their respective Hough modes are different. Considering the facts that temperatures critically determine chemistry, composition, and dynamics of the middle and upper atmosphere, and directly reflect the impacts of solar radiation and Joule heating, the information of temperature tides is therefore important and greatly needed, especially in the polar regions. Airglow imagers can also observe temperature tides [*Hernandez et al*., 1993; *Azeem and Sivjee*, 2009] but only at the emission altitude of the species and thus are incapable of providing tidal vertical profiles. Lidar observations at Davis Station (69°S) in the Antarctic have provided a vertical profile of temperature tides in the summer [*Lübken et al*., 2011]. Contrary to the conventional understanding that temperature tides are small in the polar region, *Lübken et al*. [2011] report that tides can induce a nonnegligible temperature oscillation (up to 6 K) in the summer Antarctic mesopause region, although the tidal characterization was limited to a narrow altitude range (84–96 km).

A significant gap remains in observing and understanding temperature tides over a large-altitude range in the Antarctic. Long-duration, large-altitude range, and high-resolution lidar measurements on temperatures can be used to fill in this gap. In this paper, we provide the first report and characterization of the amplitudes and vertical wavelengths of temperature tides in the Antarctic winter from 30 to 110 km using the 2 year lidar measurements in 2011 and 2012 at Arrival Heights, McMurdo (77.8°S, 166.7°E) [*Chu et al*., 2011a, 2011b]. The lidar deployed is an iron (Fe) Boltzmann temperature lidar using pulsed alexandrite lasers (see details in *Chu et al*. [2002] and *Wang et al*. [2012]). It has an exceptionally large-altitude coverage of temperatures from 30 to ~110 km, and during thermospheric Fe layer events it can even measure temperatures from 30 to 150 km [*Chu et al*., 2011b].

Revealing tides from such high latitude like McMurdo is not trivial because large-amplitude inertia-gravity waves (IGWs) in the mesosphere and lower thermosphere (MLT) [*Chen et al*., 2013] and planetary waves (PWs) in the stratosphere [e.g., *Lu et al*., 2013; *McDonald et al*., 2011; *Alexander and Shepherd*, 2010; *Randel*, 1988; *Andrews et al*., 1987] can contaminate the tidal signals. We apply a composite-day method to extract tides from numerous waves present in the Antarctic winter and develop a forward model to assess the aliasing effects from IGWs and PWs. The new features discovered include the rapid growth of diurnal and semidiurnal tidal amplitudes above 100 km and the larger tidal amplitudes and faster growth rates in the lower thermosphere corresponding to larger *Kp* indices. Simulations from the Whole Atmosphere Model (WAM) compare reasonably well with lidar observations despite some discrepancies. Consequently, WAM is used as a reference to reveal the dominant components of diurnal and semidiurnal tides in the Antarctic winter.

2. Lidar Observations and Data Analysis

2.1. Lidar Data and Composite-Day Analysis

The University of Colorado lidar group is conducting a lidar observational campaign at Arrival Heights (77.83°S, 166.67°E), McMurdo on Ross Island. This campaign is a collaboration between the United States Antarctic Program and Antarctica New Zealand. Since the first data collection in December 2010, observations have been ongoing for over 2.5 years. The Fe Boltzmann lidar deployed in the campaign is capable of temperature measurements during both day and night, leading to full diurnal data coverage. Temperatures were derived from 30 to 70 km using the Rayleigh integration technique [*Hauchecorne and Chanin*, 1980] and from 80 to 110 km using the Fe Boltzmann technique [*Gelbwachs*, 1994]. The gap between 70 and 80 km exists because neither the Rayleigh nor the Fe signal level is sufficient to derive accurate temperatures in this region. For convenience, we name the 30–70 km and 80–110 km regions as the Rayleigh region and Fe region, respectively.

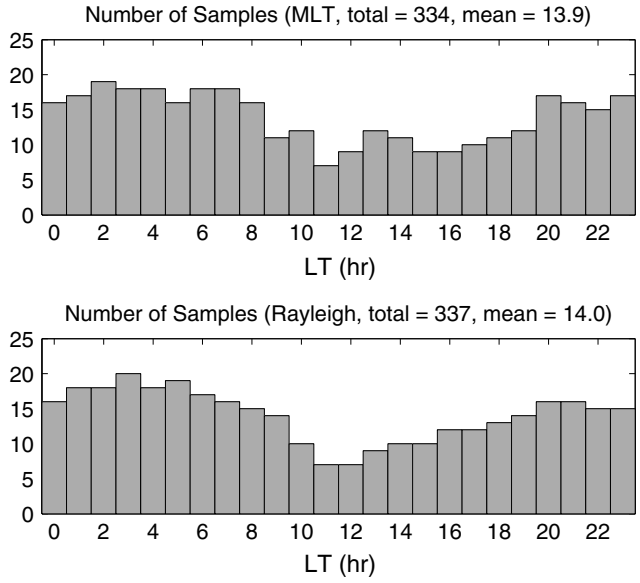

Figure 1. Diurnal distribution of hourly lidar data samples taken from May through August in 2011 and 2012 at McMurdo, separated into the (a) MLT and (b) Rayleigh regions. These data are used to compile temperature perturbations for the winter season. The total numbers of hourly samples are 334 and 337 for the MLT and Rayleigh regions, respectively.

The data used in this study were collected during the Antarctic winters (from May through August) in both 2011 and 2012 when the solar elevation was low. Such low background leads to high-quality temperature measurements. We further screen the data and remove outliers that have low signal-to-noise ratios, usually due to clouds. The 334 h of high-quality data used in this study are distributed as follows: May (93 h), June (122 h), July (57 h), and August (62 h). The raw lidar data of photon counts were recorded in resolutions of 1 min and 48 m. In the current tidal study, we reduce the temperature resolutions to 1 h and 1 km. At these reduced resolutions, typical measurement uncertainties of single temperature profiles are less than 1 K in the altitude ranges of 30–55 and 83–100 km but vary between 1 and 10 K in the ranges of 55–70, 80–83, and 100–110 km.

As mentioned earlier, a major challenge of the tidal analysis at this high southern latitude is interference from IGWs in the MLT region and PWs in the stratosphere. IGWs are strong and frequently observed at McMurdo with dominant wave periods ranging between 4 and 9 h [*Chen et al*., 2013]. The observed amplitudes of IGWs are usually on the order of 10–20 K and these waves can last over 20 h. In addition, *Lu et al*. [2013] reported that the eastward propagating PWs (relative to the ground) with periods of 1–5 days are prominent and long-lived in the winter stratosphere at McMurdo. Such PWs can induce temperature increases/decreases on the order of 10–20 K within a day, which have been frequently detected by the Fe lidar in the stratosphere at McMurdo. Furthermore, there are also reports of quasi-stationary PWs and long-period PWs in the Antarctic region [e.g., *Alexander and Shepherd*, 2010; *Randel*, 1988; *Andrews et al*., 1987]. The aliasing signal from these large-amplitude waves must be sufficiently suppressed before tidal waves can be reliably derived. Fortunately, despite the large amplitudes of IGWs and PWs, their phases are incoherent from day to day, unlike the forced tidal waves that are coherent over long periods of time. Therefore, we use the composite-day method to significantly reduce the incoherent wave effects while preserving the coherent tides.

A composite day of data covers a diurnal cycle (24 h) obtained through averaging either the absolute temperature measurements or temperature perturbations in the same local time (LT) and at the same altitude bin on different days within a chosen period, e.g., 1 month or the winter season. More data samples in the same time and altitude bin result in better suppression of the incoherent waves, in addition to reduce the measurement uncertainty of temperature for each bin. If the original temperature uncertainty at 1 h and 1 km resolutions is ΔT and the number of independent samples is N for a bin, the temperature uncertainty of this bin after averaging over these samples is given by $(\Delta T)_{\text{ave}} = \Delta T/\sqrt{N}$. The diurnal distribution of the sample numbers for the two winters in both Fe and Rayleigh regions are plotted in Figure 1. The minimum number of temperature samples is 7 at 11 LT in both regions, and the maximum number of samples is 19 at 2 LT for the 80–110 km and 20 at 3 LT for the 30–70 km. The mean number of temperature samples for each hour of the day through the cumulative May–August period in two winters is about 14. For this amount of data, there are sufficient samples over the winter season to derive the tides but not for each individual month. Therefore, we use the two winter data to compose a 24 h day and study the winter temperature tides, instead of monthly tides.

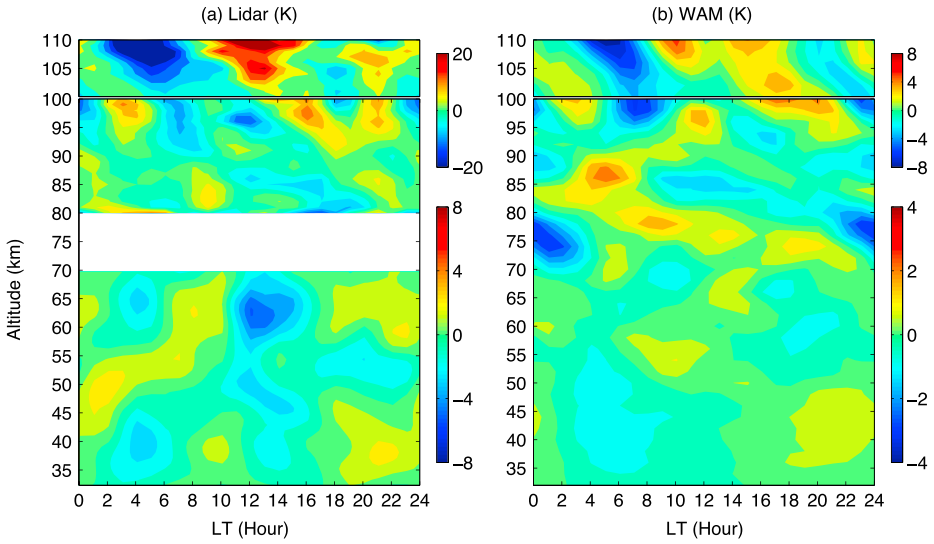

Figure 2. Hamming-smoothed composite contours of temperature perturbation for a 24 h cycle from (a) the observations of an Fe Boltzmann temperature lidar at McMurdo (77.8°S) from May to August of 2011 and 2012 and (b) 4 months of WAM output from May to August. The full Hamming window width is 5 h. The temperatures below and above 100 km are indicated by the bottom and top color bars, respectively.

To form a composite day of temperature perturbations for the winter season, we first derive the composite day of temperature perturbations for each month via subtracting the monthly mean temperature from the monthly composite. A total of eight monthly composite days of temperature perturbations in the 2 years are then averaged to obtain the winter composite day of temperature perturbations. A Hamming window with a full width of 5 h is then applied to further suppress the high-frequency structures that remain in the temperature perturbations. The smoothed temperature perturbations are shown in Figure 2a with resolutions of 1 h and 1 km. Compared to the individual day of temperature perturbations illustrated in *Chen et al*. [2013, Figure 1], the IGW signatures have been significantly reduced in Figure 2a.

However, as long as the temperature perturbations induced by IGWs and PWs can be folded into the 24 h composite day and have spectral components close to tidal periods, the aliasing effects from IGWs and PWs can be nonnegligible since their spectral leakages to diurnal and semidiurnal tides can still exist. Thus, a forward model is built to assess the aliasing impact caused by IGWs and PWs (see Appendix A) and help answer the question of how the large amplitude and phase incoherence of IGWs and PWs balance out each other and result in the overall uncertainties in deriving diurnal and semidiurnal tides. Forward model results will be discussed in conjunction with the lidar results in the following sections. But in short, we have found that the aliasing effects are negligible by applying the composite-day method and 5 h Hamming smoothing.

2.2. Tidal Amplitudes, Phases, and Vertical Wavelengths

In Figure 2a, it can be seen that the temperature perturbations of the winter composite vary between 3 and 6 K below 100 km while the perturbations increase rapidly above 100 km. The ridge-to-trough magnitudes of perturbation can reach nearly 40 K above 105 km. Also, downward phase progressions are clearly seen in the MLT region, indicative of upward propagating waves. Moreover, tidal signatures, i.e., the diurnal and semidiurnal variations, are appreciable in both the Rayleigh and Fe regions. For instance, in the Rayleigh region, considerable diurnal variations can be found between 50 and 55 km, with a cold phase before midnight (LT) and warm phase after that; semidiurnal variations can be found between 35 and 42 km, with a warm phase at about 9 and 21 LT. In the Fe region, semidiurnal variations can be seen around 95 km, with two cold phases found at 0 and 12 LT.

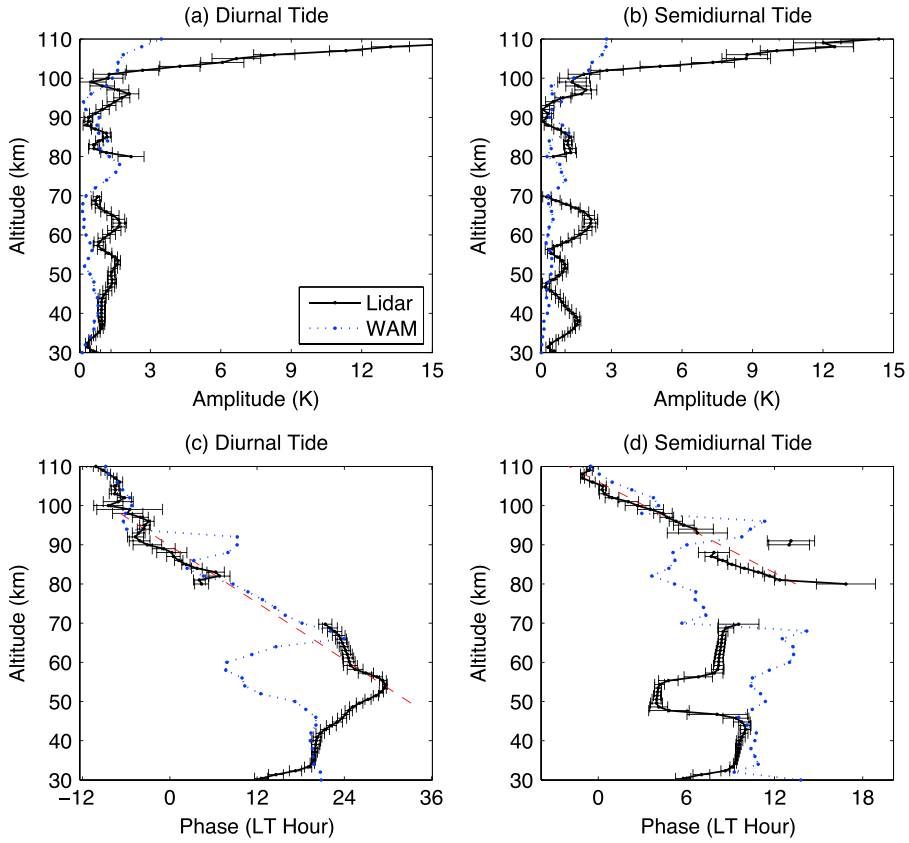

Figure 3. Diurnal and semidiurnal tidal amplitudes and phases of lidar observations (black solid lines) and WAM (blue dotted lines) derived from the temperature perturbations in Figures 2a and 2b. Here phases are defined as the local time of maximum temperature perturbations. The red dashed lines in Figures 3c and 3d correspond to linear fits of lidar tidal phases from 50 to 100 km and 80 to 110 km for diurnal and semidiurnal tides, respectively.

To delineate diurnal and semidiurnal tidal amplitudes and phases, we apply a harmonic fitting model comprising a mean temperature plus a diurnal tide and a semidiurnal tide to the composite data set shown in Figure 2a:

$$\widehat{T}(z,t) = T_o(z) + A_{24}(z)\cos\left[\frac{2\pi}{24}(t - P_{24}(z))\right] + A_{12}(z)\cos\left[\frac{2\pi}{12}(t - P_{12}(z))\right] \quad (1)$$

where T_o is the diurnal mean, A_{24} and A_{12} are the amplitudes, and P_{24} and P_{12} are the phases of the diurnal and semidiurnal tides, respectively. Tidal phase is defined as the local time when temperature reaches the maximum. The obtained tidal amplitudes and phases are plotted in Figure 3. In general, lidar-observed diurnal and semidiurnal tidal amplitudes are less than 3 K from 30 to 100 km and rapidly increase with altitude above 100 km. The mean amplitudes in the Rayleigh region are 1.1 K and 1.2 K for diurnal and semidiurnal tides, respectively. The counterparts are 1.1 K and 1.0 K in the altitude range of 80–100 km. We feed these mean tidal amplitudes into the forward model (Appendix A) as the parameters of the diurnal and semidiurnal tidal amplitudes and find that the aliasing effects of IGWs in the Fe region on the diurnal and semidiurnal tides are about 10% and 30% (~0.1 K and ~0.3 K), respectively. Meanwhile, the effects of PWs in the Rayleigh region are about 33% and 10% (~0.3 K and ~0.1 K), respectively. It is expected that when the tidal amplitudes are small, the relative aliasing effects from the IGWs and PWs would be large and vice versa. When the tidal amplitudes equal 2 K, the forward model shows that the aliasing effects from IGWs and PWs decrease to less than half of the percentages presented above. It should be noted that while the Hamming window applied to the temperature perturbation contour helps reduce the aliasing effects from IGWs, it might slightly reduce the tidal amplitudes. Our test indicates that the tidal amplitudes

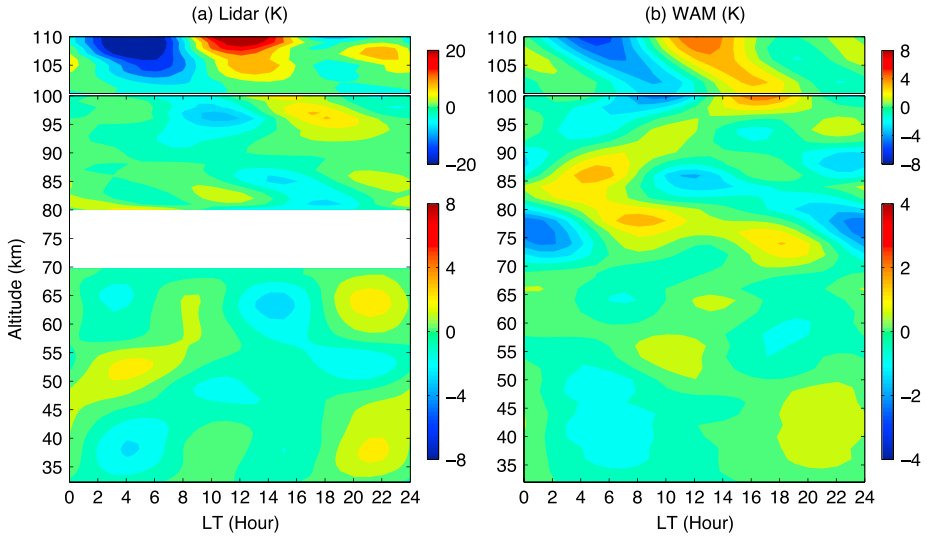

Figure 4. Reconstructed (a) lidar and (b) WAM temperature perturbations based on the diurnal and semidiurnal tidal amplitudes and phases in Figure 3. The temperatures below and above 100 km are indicated by the bottom and top color bars, respectively.

derived from the unsmoothed perturbation contour are about 3% and 10% larger than the amplitudes in Figure 3 for diurnal and semidiurnal tides, respectively.

As for tidal phases, the Fe region is characterized by downward phase progression in general and thus upward energy propagation. In Figures 3c and 3d, downward phase progressions can be found from 50 to 110 km and 80 to 110 km for the diurnal and semidiurnal tides, respectively. A few outliers of semidiurnal tidal phases around 90 km are likely due to the small tidal amplitudes at the corresponding altitudes shown in Figure 3b. The vertical wavelength estimated from the phase line is 29.0 km between 50 and 100 km for diurnal tides and 23.0 km between 80 and 110 km for semidiurnal tides (red dashed lines in Figure 3c and 3d). The reason that 100–110 km is excluded when estimating the vertical wavelength of diurnal tide is because the slope of the diurnal tidal phase line becomes steeper above 100 km. From 100 to 106 km, the phases of the diurnal tide are nearly constant with altitudes (see Figure 5b in section 2.3 for detailed phase structures between 100 and 110 km). Applying a linear fit to the phases between 100 and 110 km, the obtained vertical wavelength λ_z is about 116 km. Although such a λ_z obtained from the 10 km range is not reliable, its large value supports the conclusion that the λ_z above 100 km is much longer than that below 100 km. As for the tidal phases in the low Rayleigh region, there is no obvious vertical phase tilting for both diurnal and semidiurnal tides, which indicates long vertical wavelengths.

The fitting uncertainties of lidar tidal amplitudes and phases are plotted as error bars in Figure 3. The uncertainties of both diurnal and semidiurnal tidal amplitudes vary between 0.1 and 2 K from 30 to 110 km, while the phase uncertainties vary between 0.2 and 3 h. The method to estimating the fitting uncertainties is briefly described in Appendix B. It can be seen that the tidal phase uncertainties tend to be large when the corresponding tidal amplitudes are small. An illuminative example is the semidiurnal tidal phase uncertainties around 90 km (Figure 3d), for which the phase uncertainties are larger than those of the adjacent altitudes.

In order to quantify the overall effects of diurnal and semidiurnal tides on the temperature variations, the lidar temperature perturbation contours are reconstructed from the diurnal and semidiurnal tidal amplitudes and phases derived above and are shown in Figure 4a. In general, Figure 4a captures the major features of the temperature perturbations illustrated in Figure 2a. For example, the warm phase around 11–15 LT and the cold phase around 3–7 LT near 110 km are well reproduced in the reconstruction. The phase pattern in the Rayleigh region is strikingly similar to that in Figure 2a. It is understandable that higher-frequency features are missing from the tidal reconstruction plot, which account for the differences between Figure 2a and the

reconstruction plot. In the context of wintertime averages, diurnal and semidiurnal tides together can give rise to temperature perturbations of ~3–4 K in both the Rayleigh and lower Fe (80–100 km) regions in Figure 4a. Above 100 km, amplitudes of temperature perturbations increase rapidly and can reach over 20 K. Figure 4a reproduces the lidar-observed temperature perturbations reasonably well, indicating that the tidal amplitudes and phases are derived correctly from the winter data.

2.3. Fast Growth of Tidal Amplitude From 100 to 110 km

The rapid increase of tidal amplitudes between 100 and 110 km observed by lidar (Figures 3a and 3b) is intriguing. To quantify the growth rate of tidal amplitudes, we compare the observed scale heights of relative diurnal and semidiurnal tidal amplitudes between 100 and 110 km with that of the freely propagating wave. The scale heights of the tides observed by lidar are calculated by fitting the data with an exponential function defined as

$$A'(z) = a \exp\left(\frac{z - z_0}{2H_{\text{obs}}}\right). \tag{2}$$

where A' denotes the relative tidal amplitude defined as the absolute tidal amplitude divided by the background temperature, H_{obs} denotes the scale height, and a is the relative amplitude at a reference altitude z_0. On the other hand, the scale height of the freely propagating wave is equal to the atmospheric density scale height that is given by

$$H = \frac{kT}{Mg}, \tag{3}$$

where T denotes the mean background temperature observed by lidar, and k, M, and g are the Boltzmann constant, molecular mass, and gravitational acceleration, respectively. The fitted scale heights of lidar diurnal and semidiurnal tides between 100 and 110 km are 2.7 ± 0.1 km and 3.7 ± 0.5 km, respectively, which are smaller than the scale height of the freely propagating wave, 6.1 ± 0.6 km (see Table 1 for details). The smaller scale heights from lidar observations lead to faster amplitude increases than the freely propagating wave. Such a situation is demonstrated in Figure 5a where the blue solid line is the diurnal tidal amplitude observed by our lidar (the same as shown in Figure 3a between 100 and 110 km and is termed as "all observation group" here) and the green dashed line is an example of the freely propagating wave, which takes lidar diurnal tidal amplitude at 100 km as the reference altitude. The faster growth of the blue curve than the green curve in Figure 5 implies that, in addition to the upward propagating tides from the lower atmosphere ($<$ 100 km), there may exist other tidal sources either in situ or above this region.

From the above results, we characterize the increase of the tidal amplitudes above 100 km observed by lidar as "fast growth" because the growth rates of the tidal amplitudes exceed that of a freely propagating wave. We believe that the observations above 100 km are realistic since the estimated uncertainties are not large between 100 and 110 km (~1–2 K), and the aliasing effects from IGWs are also trivial compared with the increased tidal amplitudes in this altitude range.

Several theoretical and model studies show that thermal tides at high latitudes are dominated by the interference of upward propagating tides with tides excited by in situ solar forcing and those by the auroral momentum and energy inputs [*Fuller-Rowell et al.*, 1991; *Fesen et al.*, 1993]. Given that McMurdo is located at such a high geomagnetic latitude (~80°S), we investigate the possible link between geomagnetic activity and temperature tides by separating the lidar observations into different groups according to the different *Kp* indices, i.e., $Kp \le 1$ and $Kp \ge 2$ (Figure 5). Similar to the "all lidar observation" group, both diurnal tidal amplitudes of $Kp \le 1$ and $Kp \ge 2$ groups start to increase above 100 km and the growth rates are also greater than that of the freely propagating wave. We summarize the fitted scale height calculated by equation (2) and also the rate of amplitude increase by linear fit for each group in Table 1. Figure 5a and Table 1 demonstrate that the growth rates of the diurnal tidal amplitudes become larger as the level of geomagnetic activity increases. Interestingly, it also shows that the fast growth of tidal amplitude exists even when the geomagnetic activity is minimum (i.e., $Kp \le 1$). It is worth mentioning that the portions of the data devoted into $Kp \le 1$ and $Kp \ge 2$ groups are about 51.5% and 41.6%, respectively, of the total 334 h. Also, the data of both groups are fairly evenly distributed in the years 2011 and 2012; thus, the effects of interannual variability of the tidal amplitudes can be neglected here. The tidal phase lines above 100 km for the three *Kp* conditions are plotted in Figure 5b. As noted earlier, the phase line for "all observations" is nearly vertical or slightly

Table 1. Scale Height and Rate of Increase of Diurnal Tidal Amplitudes Between 100 and 110 km

	Scale Height[a] (km)	Rate of Increase[b] (K/km)
	Lidar Observations	
All observations	2.7 ± 0.1	1.8 ± 0.3
$Kp \le 1$	3.0 ± 0.3 (4.0 ± 0.5)[c]	1.1 ± 0.3 (0.9 ± 0.2)[c]
$Kp \ge 2$	2.4 ± 0.1	2.8 ± 0.3
Freely propagating waves	6.1 ± 0.6[d]	0.35 ± 0.02[e]
	WAM Model	
Winter	8.0 ± 1.0	0.20 ± 0.05
Summer[f]	5.9 ± 0.4	0.48 ± 0.06

[a]Scale height is defined in equation (2).
[b]Rate of increase is defined by a linear fit to the tidal amplitude between 100 and 110 km.
[c]The values quoted in the parentheses are derived in the altitude range of 100–109 km, while the numbers outside the parentheses are for the altitude range of 100–110 km.
[d]The scale height of a freely propagating wave is calculated as equation (3) using the background temperature measured by lidar. The calculation is repeated for every 1 km between 100 and 110 km. The mean and standard deviation of the results are quoted here.
[e]The rate of increase is obtained from a linear fitting to the freely propagating tide shown in Figure 5.
[f]The altitude range for WAM summer data is from 90 to 110 km.

upward from 100 to 106 km and then it becomes downward progression. Interestingly, the phases of $Kp \le 1$ and $Kp \ge 2$ have turning points around 106 and 102 km, respectively, where the phases are upward below the turning points but become downward above the points.

3. Comparison With WAM and Dominant Components of Tides

3.1. Comparison With WAM-Resolved Tides

The lidar observations are compared with a sophisticated general circulation model, WAM. WAM extends from the surface to about 600 km and is built on an existing operational Global Forecast System (GFS) model [*Akmaev et al.*, 2008; *Fuller-Rowell et al.*, 2008, 2010] to study the dynamical links between the lower and upper atmosphere. WAM is a spectral model and was run at the moderate T62 spectral resolution corresponding to about 1.8° × 1.8° in latitude-longitude for the present simulations. The vertical extension of the model domain requires the addition of physical processes operating in the neutral upper atmosphere such as radiative transfer under the breakdown of local thermodynamic equilibrium, heating by solar ultraviolet and extreme ultraviolet radiation, mutual diffusion of major neutral species, and interaction with the ionosphere through ion drag and Joule heating. The grazing incidence integral [*Rishbeth and Garriott*, 1969] is used to treat the solar heating at very high latitudes when the zenith angle is close to 90°. Tidal forcing by solar radiation at very high latitudes tends to drive quite small tidal wind and temperature amplitudes [*Fesen et al.*, 1993] compared to tides propagating from the lower atmosphere or from geomagnetic activity.

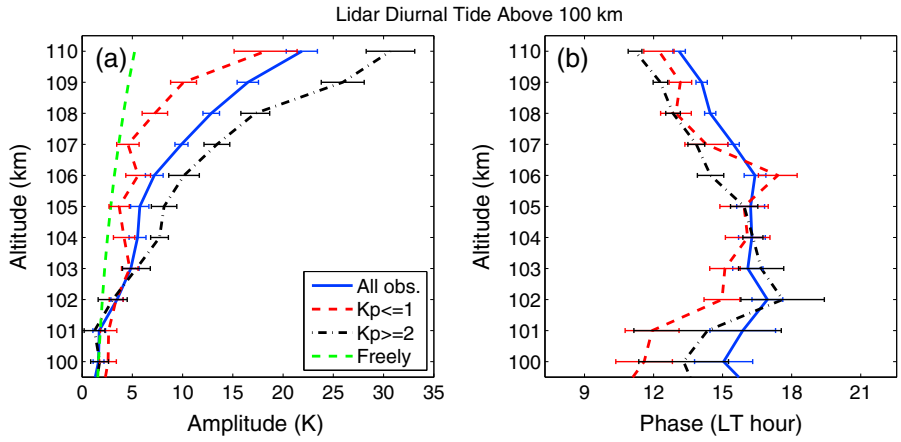

Figure 5. Lidar diurnal (a) tidal amplitudes and (b) phases from 100 to 110 km based on the different *Kp* indices. The freely propagating tidal amplitude is also plotted as a green dashed line in Figure 5a for comparison.

For the study reported here, the model is first initialized and then allowed to run freely for a model year to produce a "free" unconstrained annual run. No variation in external forcing was imposed, but the model has all the natural internal variability expected of a tropospheric weather model. In the region of overlap, a GFS run was used to initialize the model; above the GFS upper boundary at about 62 km, WAM was initialized by empirical temperature and neutral composition fields from the NRLMSISE-00 model [*Picone et al*., 2002]. After about 2 months of simulation, the specific initial conditions are not apparent. Thus, the simulation results are considered as model climatology rather than as corresponding to a specific period [*Fuller-Rowell et al*., 2008, 2010]. The WAM model has also been incorporated into the operational Gridpoint Statistical Interpolation data assimilation system, which enables the model to follow the dynamics of specific periods and forecast real weather events, such as sudden stratospheric warmings [*Wang et al*., 2011; *Fuller-Rowell et al*., 2011].

The WAM simulation used for this study is for a very low level of geomagnetic activity, with the electric field specified by the Weimer electric field model [*Weimer*, 2005] for condition at the $Kp = 1$ level. This particular WAM simulation has no auroral precipitation. WAM has shown to be capable of resolving atmospheric tides to a great extent [*Akmaev et al*., 2008; *Akmaev*, 2011]. In our study, 4 months (May–August) of WAM temperatures from a single-year run with a temporal resolution of 1 h and vertical resolution of 2 km were selected to derive the composite day of temperature perturbations using the same method as lidar data. The Hamming-smoothed results are shown in Figure 2b.

Similar to Figure 2a, tidal signatures are appreciable in Figure 2b and there is a certain resemblance of the wave patterns between lidar and WAM. For instance, in both data sets, two warm phases propagate downward from 110 km around 11 and 23 LT to 90 km; from 30 to 50 km, warm phases are found before midnight (0 LT) and cold phases after that. This agreement is better illustrated in the comparison of the reconstructed temperature perturbations (Figure 4). As discussed earlier in section 2.3, Figure 4a captures the major features of the smoothed temperature perturbations illustrated in Figure 2a. This is also true for the WAM simulations by comparing Figures 2b and 4b. A noticeable discrepancy between lidar and WAM is found at altitudes of 60–70 km, where several hours of phase shift exist between lidar and WAM. Nevertheless, WAM generally reproduces the observed tidal patterns, especially the phases between 90 and 110 km and between 30 and 50 km.

A closer inspection of Figures 4 reveals that the magnitudes of temperature perturbations induced by tides in WAM are approximately half of those in lidar observations at the same altitudes. It should be noted that the total hours used in WAM (2952 h in 4 months of 1 year) is about 8.8 times the total lidar hours (over 330 h), which will suppress the incoherent components more effectively. In order to study whether the smaller temperature perturbations resolved in WAM are due to a larger total sampling or a real underestimation, we randomly selected a continuous period between May and August and obtain temperature perturbations in WAM. For each period, it includes the same number of data points as lidar. It is found that by using the same data hours, WAM temperature perturbations become comparable with lidar below 100 km, whereas they are still less than half of the lidar perturbations between 100 and 110 km, no matter what periods are chosen for the comparison. This implies an underestimation of tides by WAM in the altitude range of 100–110 km.

The same harmonic model of equation (1) is applied to the composite day of WAM temperature perturbations (Figure 2b), and the results are also shown in Figure 3. The 4 month mean tidal amplitudes in WAM are normally less than 2 K below 100 km, in general, smaller than the lidar, which are not unexpected as discussed in the last paragraph. An amplitude-increasing trend above 100 km is noticeable but with an underestimated magnitude and a much slower growth rate (Table 1). The lidar diurnal and semidiurnal tidal amplitudes are about 13.2 K and 12.5 K at 108 km, while the values are 2.6 K and 2.8 K for WAM, respectively. The scale height of the amplitude increase in WAM winter is 8.0 ± 1.0 km, which is larger than that of freely propagating wave (6.1 ± 0.6 km) and much larger than lidar observations (2.7 ± 0.1 km). This indicates that the tidal amplitude increases much more slowly in the WAM simulation. However, it is worth mentioning that the amplitude growth rate simulated by WAM in summer (derived in the same way as the winter counterpart except that months are chosen from November to February) is faster compared to winter. The relative temperature perturbations (defined as absolute temperature perturbations divided by the mean temperature) show considerable amplitude increases at altitudes of 86–118 km for the diurnal tide and 82–100 km for the semidiurnal tide, respectively (Figure 6). The scale height of amplitude increase in summer, 5.9 ± 0.4 km, is slightly smaller than that of the freely propagating wave, although it is still larger than that derived from lidar data.

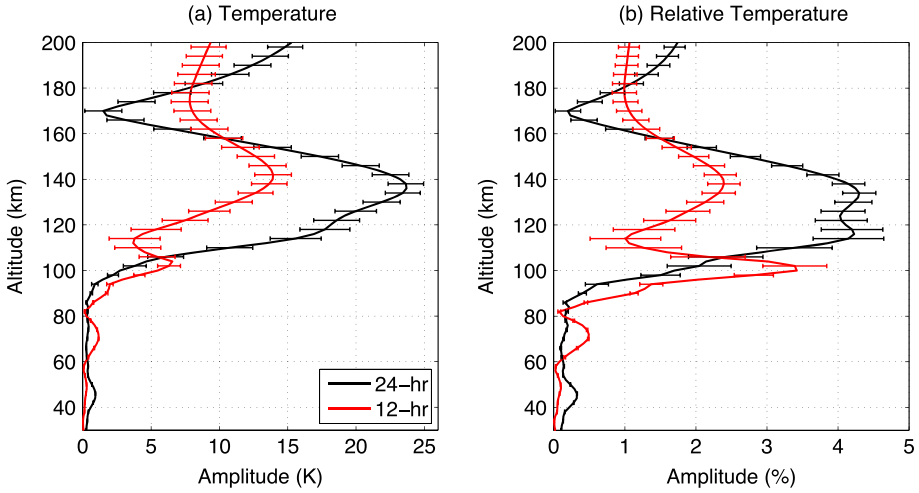

Figure 6. Summer mean tidal amplitudes in (a) temperature and (b) relative temperature perturbations from WAM. Black lines are the diurnal tide, and red lines are the semidiurnal tide. The error bars are the uncertainties of tidal amplitudes estimated by the same method as lidar data (see the details in Appendix B).

The WAM tidal phases agree with lidar observations above 100 km in general, as shown in Figures 3c and 3d. The phase agreements between lidar and WAM are also illustrated in the reconstructed tidal perturbations as discussed earlier in this section. It is suggested that WAM captures part of the underlying mechanisms, giving rise to tides between 100 and 110 km, but the total magnitudes need to somehow be augmented in winter. The consistency between the diurnal tidal phases is also found at altitudes below 100 km except for the ranges of ~85–90 km and ~45–60 km. The consistency for the semidiurnal tide is found below ~48 km and above ~97 km, while between 48 and 70 km, a phase difference of 3.8–7.4 h exists. Overall, WAM reproduces many of the features found in lidar observations.

3.2. Dominant Components of Tides

It is well known that tides observed from a single station are the superposition of migrating and nonmigrating tides [*Oberheide et al.*, 2006; *Lu et al.*, 2011]. Since WAM simulations show multiple consistencies with lidar observations, we apply WAM to provide a reference on the dominant tidal components at McMurdo. The WAM temperatures at 77.2°S (the closest latitude to McMurdo) are selected to compute the composite day of

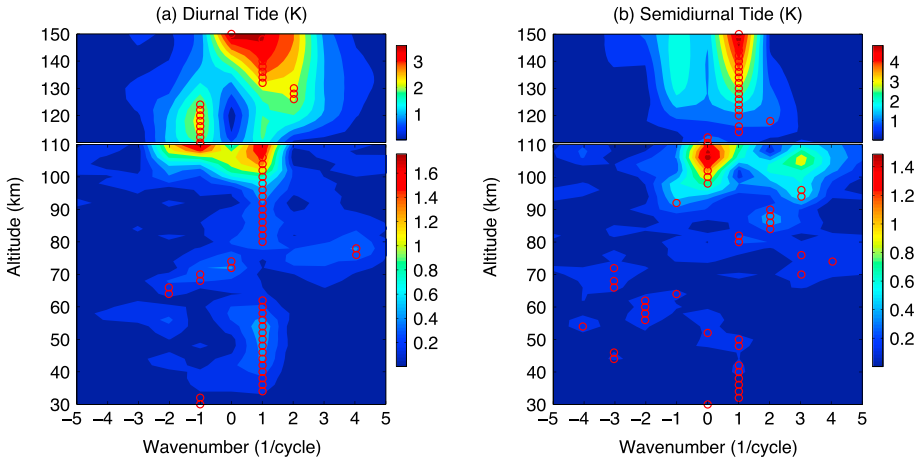

Figure 7. Amplitude spectra of (a) diurnal and (b) semidiurnal tides at 77.2°S from WAM. The wave numbers with the largest amplitudes at each altitude are marked with red circles. Positive wave numbers correspond to westward propagating tidal components, while negative wave numbers correspond to eastward propagating components. Zero wave numbers indicate nonpropagating tidal components that are zonally symmetric.

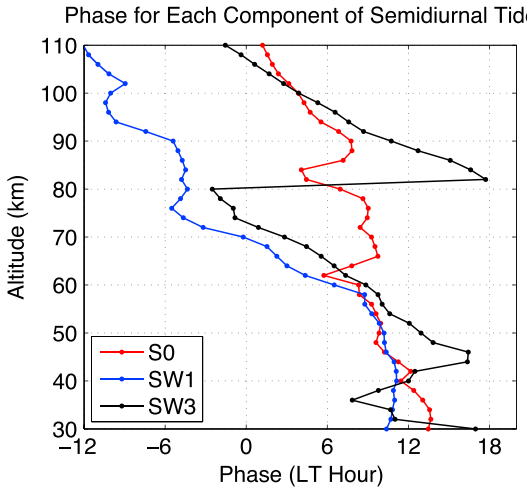

Figure 8. Phases for S0, SW1, and SW3 components of the semidiurnal tide from WAM.

temperature perturbations at different longitudes. Then a 2-D fast Fourier transform is applied to the composited temperature perturbations as functions of time and longitude, from which the amplitude spectra with respect to wave number and frequency are inferred for each altitude.

Figure 7 shows that the dominant component of the diurnal tide in WAM is the DW1 (westward propagating diurnal tide with wave number 1) from 30 to 110 km, which suggests that this component is likely to be the dominant diurnal tidal component observed at McMurdo. For the semidiurnal tide, two nonmigrating components S0 and SW3 are stronger than the other components between 90 and 110 km, where the phase of S0 changes approximately from ~7 to 1 LT and that of SW3 changes from ~11 to −1 LT (Figure 8). Thus, the vertical wavelengths of S0 and SW3 in this altitude range are estimated to be 40 and 20 km, respectively. Interestingly, the corresponding lidar observations of semidiurnal tidal phase in this altitude range (Figure 3d) are close to WAM prediction of the SW3 phases. In addition, the estimated vertical wavelength of ~23.0 km for the semidiurnal tide matches better with that of SW3 (i.e., ~20 km) than S0. Therefore, SW3 is more likely to be the dominant component of the semidiurnal tide between 90 and 110 km at McMurdo. In the altitude range of 30–45 km, the phases of the semidiurnal tide largely follow those of SW1 (Figures 3d and 8), which supports the WAM prediction that SW1 is the strongest component in this altitude range. Similarly, based on the temperature observations made by MLS on UARS in the winter MLT region at 86 km, *Forbes and Wu* [2006] report that the dominant diurnal component is DW1 from ±60°–70° and the semidiurnal components SW1, SW2, and SW3 have comparable amplitudes with each other at ±60°.

One possible source of the nonmigrating semidiurnal tides (i.e., SW1 and SW3) is the nonlinear interaction of quasi-stationary PW wave number 1 and the migrating semidiurnal tide SW2. This mechanism can generate nonmigrating semidiurnal tides in winds in Antarctica, and the dominant component is SW1 [*Forbes et al.*, 1995; *Baumgaertner et al.*, 2006; *Murphy et al.*, 2006]. Nevertheless, the WAM simulation shows that the SW2 component in temperature is very weak at McMurdo. Thus, according to WAM, the local nonlinear interaction of SW2 and PWs is unlikely to be the mechanism generating SW1 and SW3. It does not exclude, however, the possibility that SW1 and SW3 are generated by the nonlinear interaction elsewhere and then propagate to McMurdo [*Angelats i Coll and Forbes*, 2002; *Yamashita et al.*, 2002; *Baumgaertner et al.*, 2006].

A key difference between the diurnal and semidiurnal tides in Figure 7 is that the migrating component DW1 dominates the diurnal tide more uniformly with altitude, while multiple nonmigrating components of the semidiurnal tide such as SW1, SW3, SE1, and SE2 dominate at different altitude ranges below 90 km. The scattered dominance pattern for the semidiurnal tide and resulting irregular phases between 50 and 90 km shown in both WAM and observations make it difficult to estimate a single vertical wavelength in this region. So this is why we focus on the altitude range of 80–110 km to provide the lidar estimation of the vertical wavelength for the semidiurnal tide, where the downward phase progression seems obvious and linearly changing with altitude. From the reference provided by WAM that different tidal components could dominate at different altitudes, we know that conducting reasonable simulations of tidal components especially the dominant ones is key for models to reproduce realistic tides from single-station observations.

4. Discussion

Figure 5 exhibits superexponential amplitude increases of the diurnal tides above 100 km. Larger *Kp* indices appear to correspond to larger tidal amplitudes and faster growth rates from 100 to 110 km. The slopes of tidal phases become steeper above 100 km, and the tidal phases even barely change with altitude from 100

to 106 km, although the phases turn to be downward above 106 km. The significant amplitude increases, and phase structure changes imply that there may exist additional tidal sources near or above 100 km. *Avery et al*. [1989] report vertical wavelengths of 20–40 km for wind diurnal tides below 100 km during winter months at Mawson, Antarctica (67°S), which is comparable to our results of ~29 km. In the same time, *Avery et al*. [1989] report that the wind diurnal tides at Mawson show evanescent structure and upward phase progression around 100 km. Similar phase behaviors have also been identified for high-latitude stations in the Northern Hemisphere, such as Poker Flat, Alaska (65°N) and Tromsø, Norway (69.5°N). They suggested an in situ forcing centered around 100 km for the diurnal tides at high latitudes, which is supportive of our speculation.

One possible tidal source is the geomagnetic activity as suggested by several model simulations. In the thermosphere-ionosphere general circulation model (TIGCM) simulation by *Fesen et al*. [1991], the diurnal tidal amplitudes of high-latitude temperatures in the lower thermosphere (100–150 km) show increases of 5–15 K with auroral forcings. *Fesen* [1997] shows that from 100 to 110 km, the amplitudes of diurnal temperature tides at 67.5°N increase from ~3 to ~9 K for $Kp = 1$, from ~6 to ~20 K for $Kp = 3$, and from ~10 to ~40 K for $Kp = 5$. The significant amplitude growth and correspondence of larger tidal amplitudes with higher geomagnetic activity levels are consistent with our observations. This consistency is also seen in the coupled thermosphere-ionosphere-plasmasphere model simulations [*Müller-Wodarg et al*., 2001]. From their simulations, *Müller-Wodarg et al*. [2001] suggest that (1) the in situ diurnal and semidiurnal oscillations generated at high latitudes by ion-neutral interactions such as ion drag and Joule heating are stronger than the upward propagating tides and (2) due to their geomagnetic origin, the in situ oscillations strongly depend on *Kp* index and thus cause an overall dependency with larger *Kp* index, giving rise to stronger diurnal and semidiurnal winds. It is unknown at which altitudes the Joule heating and ion drag associated with geomagnetic activity will act as a tidal source near McMurdo location. Figure 5b hints that the case of $Kp \leq 1$ has higher altitudes (~100–106 km) for nearly vertical or upward phases than the case of $Kp \geq 2$ (~100–102 km). This is consistent with a general understanding that stronger geomagnetic activity has a better chance to penetrate to lower altitudes.

On the other hand, the existences of fast amplitude growths for all *Kp* index categories including $Kp \leq 1$ imply that even though geomagnetic activity may cause an enhancement of temperature tides, other additional contributors are still needed. Two possible candidates could be direct solar heating and chemical heating in the lower thermosphere. Direct solar heating refers to the absorbed solar energy that is converted to heat immediately, while chemical heating is the heat release due to exothermic reactions [*Smith et al*., 2003]. Whereas direct solar heating occurs only during daylight thus depending on solar zenith angle, chemical heating occurs during both day and night [*Smith et al*., 2003; *Mlynczak and Solomon*, 1993]. We have examined the duration of sunlight through diurnal cycles from May to August at McMurdo (figure not shown). It is totally dark between 100 and 110 km only for a period of 3–4 weeks (centered at winter solstice). Other than that, direct sunlight exists between 100 and 110 km and lasts for up to ~13 h per day, depending on timing relative to the winter solstice. At 130 km, the totally dark situation is absent and the minimum sunlit period is ~2 h. Due to the existence of solar radiation, the periodic absorption of it can likely generate tides locally and contribute to the observed amplitude growth. On the other hand, the dominant chemical heating in the upper mesosphere and lower thermosphere is due to the exothermic reaction of $O + O \rightarrow O_2$ [*Smith et al*., 2003; *Smith*, 2004]. Such an exothermic reaction can occur during both day and night and therefore is not expected to have a pronounced diurnal cycle unless the atomic O distribution is affected by tidal transport and solar radiation. In the MLT region, atmospheric tides can cause temperature, density, and wind fluctuations, which can influence the exothermic reaction rate and atomic O density, thus the chemical heating rate. According to *Smith et al*. [2003], if the heating is stronger where the tidal temperature tendency is positive, the tide will be amplified; a stronger heating coinciding with a negative tidal temperature tendency will lead to damping of the tide. Depending on the tidal phase, chemical heating could therefore contribute to the observed amplitude growth. Furthermore, there is some evidence that the nonmigrating semidiurnal tides SW1 and SW3 in the Southern Hemisphere propagate from the Northern Hemisphere [e.g., *Angelats i Coll and Forbes*, 2002; *Yamashita et al*., 2002; *Baumgaertner et al*., 2006; *Smith et al*., 2007; *Murphy et al*., 2009]. Although such propagation is so far limited to the summer tides, other tides might propagate laterally in winter. This could be another contributor to the rapid growth of certain tides in the layer above 100 km.

The observational evidences provided by lidar measurements in the current study may shed a light on some implications and speculations about the tidal sources in the high-latitude lower thermosphere. However, due

to the lack of more extensive observations and modeling support, it should be noted that the effects of geomagnetic activity, solar heating, and chemical heating on tides need to be better understood and modeled before any conclusions can be reached concerning their roles as tidal sources responsible for the observed fast amplitude growth.

5. Conclusions

This paper presents an unprecedented study on the diurnal and semidiurnal thermal tides in temperature from 30 to 110 km in the winter at McMurdo, Antarctica, using 2 years of the Fe Boltzmann lidar observations. Antarctic winter is a dynamic period with large PWs in the stratosphere [e.g., *Lu et al*., 2013; *Alexander and Shepherd*, 2010; *Randel*, 1988; *Andrews et al*., 1987] and extraordinary IGWs in the MLT region [*Chen et al*., 2013]. These strong waves make it challenging to study thermal tides. Our lidar data show that the mean wintertime amplitudes of diurnal and semidiurnal tides are generally small below 100 km (less than 3 K) and do not increase significantly with altitude. Forward modeling demonstrates that the aliasing effects from PWs and IGWs on tides are less than 0.3 K, and it also shows that the relative effects become smaller when tidal amplitudes become larger. Despite small amplitudes below 100 km, phase structures of tides are reasonable and amplitude errors are small in most altitudes. Therefore, we conclude that the obtained tidal amplitudes are generally above noise levels and the tidal waves are authentic signatures. The vertical wavelength is estimated from the phase line to be 29.0 km between 50 and 100 km for diurnal tides and 23.0 km between 80 and 110 km for semidiurnal tides. WAM compares reasonably well with the observations below 100 km. With a reference provided by WAM, we find that the diurnal tide is likely linked to the DW1 component and the semidiurnal tide is most likely determined by SW3.

A new finding of this study is the fast growth of diurnal and semidiurnal tidal amplitudes above 100 km exceeding that of the freely propagating tides originating from the lower atmosphere. The investigation of the growth rates of tidal amplitudes by calculating the scale heights shows that the lidar-observed scale heights of both diurnal and semidiurnal tidal amplitudes are smaller than that of the freely propagating wave. Such fast growth exists for all *Kp* index cases, and larger *Kp* indices appear to be corresponding to larger tidal amplitudes and faster growth rates from 100 to 110 km. The slopes of diurnal tidal phases become steeper above 100 km, and the tidal phases even barely change with altitude from 100 to 106 km.

The fast growth of tidal amplitudes above 100 km observed by lidar is intriguing and novel for high-latitude observations. Although incoherent scatter radar (ISR) observations have shown fast increases associated with geomagnetic activity, most of them have been focused on tidal winds in the Northern Hemisphere and lower latitudes where ISR measurements are available [e.g., *Müller-Wodarg et al*., 2001]. To our knowledge, the McMurdo lidar observations provide the first report of such a phenomenon in temperature tides in the winter Antarctic region. The significant amplitude increases and phase structure changes suggest the presences of tidal sources above or near 100 km in addition to the upward propagating tides from lower atmosphere. It is noteworthy that since the tidal amplitude uncertainties and aliasing effects from PWs and IGWs are small, the fast amplitude growth observed between 100 and 110 km is a robust feature. The underestimation of the amplitude growth above 100 km by WAM is likely because the model simulation is for a very low level of geomagnetic activity ($Kp = 1$) and has no auroral precipitation, which if included would considerably enhance the conductivities in the lower thermosphere and hence the Joule heating rates from the imposed electric field. The resultant rather weak geomagnetic forcing in WAM may well explain the weak response of the diurnal and semidiurnal tides in the lower thermosphere at McMurdo.

The mechanism responsible for the fast amplitude growth of temperature tides in the lower thermosphere is an open question. Whether and how the geomagnetic activity, solar heating, and chemical heating would affect the thermal tides at such high southern latitudes (geographic ~77.8°S and geomagnetic ~80°S) are unknown. The quantitative evaluations require more observational data and modeling work. A better characterization and understanding of tides at high geomagnetic latitudes will help to assess the tidal impacts on space weather and at the same time hint at the effects of geomagnetic activity on high-latitude thermal tides.

Appendix A: A Forward Model to Assess Aliasing

A forward model adopting the Monte Carlo method is built to see how the large amplitudes and phase incoherence of IGWs and PWs balance out each other by quantifying the aliasing effects of IGWs and PWs on

Table A1. Ranges/Values of Parameters in the Forward Modeling[a]

	Amplitude A (K)	Wavelength $\lambda = 2\pi/k$ (km)	Period $T = 2\pi/\omega$ (h)	Phase ϕ (rad)
		Randomly Chosen Parameters		
IGW	10–20	20–40	4–9	$0–2\pi$
SPW ($<$ 10 days)	3–10	60–100	72–120	$0–2\pi$
LPW ($>$ 10 days)	2–4	60–100	240–1680	$0–2\pi$
		Prescribed Parameters[b]		
Diurnal tide (T_{24})	~1	30	24	0
Semidiurnal tide (T_{12})	~1	20	12	0

[a]The range of T_{bias} is from -3 to $+3$ K, and it is randomly selected for each data segment.
[b]The amplitudes of diurnal tide and semidiurnal tide are about 1 K in the MLT (80–100 km) and the Rayleigh region, according to Figure 3.

tides. This forward model assumes that the temperature perturbations are mainly contributed from the diurnal and semidiurnal tides as well as from IGWs in the altitude range of 80–110 km and from PWs in the range of 30–70 km, which can be expressed as

$$\begin{aligned} T'(z,t) = {} & A_{T_{24}} \cos\left(k_{T_{24}} z + \omega_{T_{24}} t + \phi_{T_{24}}\right) + A_{T_{12}} \cos\left(k_{T_{12}} z + \omega_{T_{12}} t + \phi_{T_{12}}\right) \\ & + A_{\mathrm{IGW}} \cos(k_{\mathrm{IGW}} z + \omega_{\mathrm{IGW}} t + \phi_{\mathrm{IGW}}) + A_{\mathrm{SPW}} \cos(k_{\mathrm{SPW}} z + \omega_{\mathrm{SPW}} t + \phi_{\mathrm{SPW}}) \\ & + A_{\mathrm{LPW}} \cos(k_{\mathrm{LPW}} z + \omega_{\mathrm{LPW}} t + \phi_{\mathrm{LPW}}) + T_{\mathrm{bias}}(z) \end{aligned} \quad \text{(A1)}$$

A, k, ω, and ϕ correspond to amplitude, wave number, frequency, and phase, respectively. The subscripts T_{24}, T_{12}, IGW, SPW, and LPW correspond to diurnal tidal wave, semidiurnal tidal wave, IGW, short-period PW, and long-period PW, respectively. Here, the SPWs have periods less than 5 days that are used to represent the prominent eastward propagating PWs observed by *Lu et al*. [2013] at McMurdo, while the LPWs have periods between 10 and 70 days that represent the quasi-stationary PWs and other long-period PWs in the stratosphere and mesosphere [e.g., *Randel*, 1988; *Andrews et al*., 1987; *Alexander and Shepherd*, 2010]. A T_{bias} term is also included to account for the possible residual seasonal trend and residual day-to-day variations caused by other waves that are not considered in the first five terms. A program is coded utilizing equation (A1) to repeatedly generate data segments that consist of diurnal and semidiurnal tidal signals as well as the IGW signal or SPW and LPW signals to simulate the derived temperature perturbation profiles in the Fe and Rayleigh regions, respectively.

To determine the aliasing effect from IGW in the Fe region, we set the amplitudes of SPW and LPW terms to zero but let the parameters associated with IGW term and T_{bias} in equation (A1) be randomly chosen by the program while keeping those associated with tidal terms fixed. The selecting ranges of amplitudes (A_{IGW}), wavelengths (k_{IGW}), and periods (ω_{IGW}) of the IGWs are determined according to the observational paper by *Chen et al*. [2013], and the range of phases (ϕ_{IGW}) is from 0 to 2π. The ranges of randomly chosen parameters and the values of the fixed parameters are summarized in Table A1. In addition, we also let the length of data segment, namely the time span t, be randomly determined by the program. Since most of the lidar data spans are between 3 and 24 h, we set the range of t from 3 to 24 h as well. Similarly, to assess the aliasing effects from SPW and LPW in the Rayleigh region, we set the IGW term to zero but let the parameters of SPW term and T_{bias} in equation (A1) be randomly chosen by the program while keeping those associated with tidal terms fixed. The selecting ranges of SPW parameters are determined according to the observational paper by *Lu et al*. [2013]. Furthermore, the amplitude for the LPW term is determined from an analysis to the Modern-Era Retrospective Analysis for Research and Applications (MERRA) data around McMurdo latitude in the winters of 2011 and 2012 (figures not shown). A fixed period between 10 and 70 days (e.g., 20, 30, 40, 50, and 60 days) is chosen for the LPW term with a fixed initial phase, but we let the data segment time span be randomly determined by the program as done in the IGW case. Different initial phases or periods of the LPW are tried for different runs of the simulation, and the aliasing effects are estimated from the average of these different runs. The parameter ranges for SPW and LPW terms are also summarized in Table A1.

By repeating the above data segment generating procedure, the program accumulates certain amount of these segments and generates a composite day of temperature perturbation contour. Similar to the lidar data processing in section 2, a Hamming window with a full width of 5 h is also applied to the simulated composite

perturbation contour. The number of segments that are needed to generate the composite day is determined when the total hours of these segments equal the total hour of lidar data shown in Figure 1 (334 h in the MLT and 337 h in the Rayleigh region). In this case, 23 data segments are accumulated for one composite contour. After the smoothed composite perturbation contour is obtained, the harmonic fitting model (equation (1)) presented in section 2 is then applied to derive the tidal amplitudes and phases at each altitude. In order to quantify the aliasing effects of IGWs and PWs, we compare the means of the diurnal and semidiurnal tidal amplitudes obtained from 300 cases of simulated temperature perturbation contours with the prescribed tidal amplitudes (A_{T24} and A_{T12}). The reason that 300 case runs are chosen for the Monte Carlo method is to ensure that the means of the tidal amplitudes converge to stable values. The forward model results are discussed in section 2.

Appendix B: Estimation of Harmonic Fitting Errors

The harmonic fitting model (equation (1)) can be rewritten as

$$\widehat{T}(t) = M + D_C \cos(\omega t) + D_S \sin(\omega t) + S_C \cos(2\omega t) + S_S \sin(2\omega t), \tag{B1}$$

where $\omega = 2\pi/24$. The relations between diurnal and semidiurnal parameters in equations (1) and (B1) are

$$T_o = M \tag{B2}$$

$$A_{24} = \sqrt{D_C^2 + D_S^2} \tag{B3}$$

$$A_{12} = \sqrt{S_C^2 + S_S^2} \tag{B4}$$

$$\Phi_{24} = \omega P_{24} = \tan^{-1}(D_S/D_C) \tag{B5}$$

$$\Phi_{12} = 2\omega P_{12} = \tan^{-1}(S_S/S_C) \tag{B6}$$

Using the least squares fit approach [*Taylor*, 1997], the fitted parameters are related to the measured temperature values as follows:

$$M = \frac{1}{n}\sum_{i=1}^{n} T(t_i) \tag{B7}$$

$$D_C = \frac{\sum_{i=1}^{n} T(t_i)\cos(\omega t_i)}{\sum_{i=1}^{n} \cos^2(\omega t_i)} \tag{B8}$$

$$D_S = \frac{\sum_{i=1}^{n} T(t_i)\sin(\omega t_i)}{\sum_{i=1}^{n} \sin^2(\omega t_i)} \tag{B9}$$

$$S_C = \frac{\sum_{i=1}^{n} T(t_i)\cos(2\omega t_i)}{\sum_{i=1}^{n} \cos^2(2\omega t_i)} \tag{B10}$$

$$S_S = \frac{\sum_{i=1}^{n} T(t_i)\sin(2\omega t_i)}{\sum_{i=1}^{n} \sin^2(2\omega t_i)}, \tag{B11}$$

where n is the number of independent data points.

The errors in the fitted parameters are assumed to be mutually statistically independent. They are related to ΔT, the deviation of the measured individual temperature T from the tidal model $\widehat{T}$ given by equation (B1). That is,

$$\Delta T(t) = T(t) - \widehat{T}(t). \tag{B12}$$

Here the deviation ΔT can be introduced by photon noise, gravity and planetary waves (nontidal waves), and the error in the tidal model (i.e., tidal components other than the diurnal and semidiurnal tides in equation (B1)). Under equal-weight fit and if we assume that the root-mean-square (RMS) temperature measurement errors are approximately the same regardless of the time of day, the RMS errors in the fitted parameters can be derived from equations (B2) to (B11) using the propagation of errors [*Taylor*, 1997]:

$$\sigma_M = \sqrt{\frac{1}{n}}\mathrm{Std}(\Delta T) \tag{B13}$$

$$\sigma_{D_C} = \sigma_{D_S} = \sigma_{S_C} = \sigma_{S_S} = \sqrt{\frac{2}{n}}\mathrm{Std}(\Delta T) \tag{B14}$$

$$\sigma_{A_{24}} = \sigma_{A_{12}} = \sqrt{\frac{2}{n}}\mathrm{Std}(\Delta T) \tag{B15}$$

$$\sigma_{\Phi_{24}} = \sqrt{\frac{2}{n}}\frac{\mathrm{Std}(\Delta T)}{A_{24}} \tag{B16}$$

$$\sigma_{\Phi_{12}} = \sqrt{\frac{2}{n}}\frac{\mathrm{Std}(\Delta T)}{A_{12}} \tag{B17}$$

$$\mathrm{Std}\left(\Delta\widehat{T}\right) = \sqrt{\frac{5}{n}}\mathrm{Std}(\Delta T). \tag{B18}$$

Note that for the tidal fit where we have a temperature sample for every hour, $n = 24$. The temperature variance $\mathrm{Var}(\Delta T) = \mathrm{Std}^2(\Delta T)$ can be estimated by computing the variance of the difference between the actual hourly temperature measurements and the fitted harmonic model.

$$\frac{1}{n}\sum_{i=1}^{n}\left[T(t_i) - \widehat{T}(t_i)\right]^2 = \mathrm{Var}(\Delta T)_{\mathrm{PN}} + \mathrm{Var}(\Delta T)_W + \mathrm{Var}\left(\Delta\widehat{T}\right) = \left(1 + \frac{5}{n}\right)\mathrm{Var}(\Delta T), \tag{B19}$$

where the first term represents photon noise induced variance, the second term represents the variance induced by nontidal waves like gravity and planetary waves, and the third term is the error in the fitted tidal model. Therefore, the temperature variance can be derived as

$$\mathrm{Var}(\Delta T) = \frac{1}{(1 + 5/n)}\frac{1}{n}\sum_{i=1}^{n}\left[T(t_i) - \widehat{T}(t_i)\right]^2 = \frac{1}{29}\sum_{i=1}^{24}\left[T(t_i) - \widehat{T}(t_i)\right]^2. \tag{B20}$$

Once $\mathrm{Var}(\Delta T)$ is computed using equation (B20), the RMS errors of the fitted parameters can be obtained from equations (B13) to (B17).

Acknowledgments

We sincerely acknowledge Wentao Huang, John A. Smith, and Zhangjun Wang for their contributions to the McMurdo lidar campaign. We are indebted to Jeffery M. Forbes for his invaluable advice. We are grateful to Wenbin Wang and Elsayed Talaat for their inspirational suggestions. We also appreciate Fei Wu and Rashid A. Akmaev for running and preparing WAM data. We thank the staff of the United States Antarctic Program, McMurdo Station, Antarctica New Zealand, and Scott Base for their support. We offer special thanks to Vladimir Papitashvili for his encouragement and help in this research. The lidar project was supported by NSF grants ANT-0839091 and PLR-1246405. X.L. sincerely acknowledges the generous support of the CIRES Visiting Fellows Program (http://cires.colorado.edu/collaboration/fellowships/). MERRA data used in this study were provided by the Global Modeling and Assimilation Office (GMAO) at NASA Goddard Space Flight Center through the NASA GES DISC online archive.

References

Akmaev, R. A. (2011), Whole atmosphere modeling: Connecting terrestrial and space weather, *Rev. Geophys.*, *49*, RG4004, doi:10.1029/2011RG000364.

Akmaev, R. A., T. J. Fuller-Rowell, F. Wu, J. M. Forbes, X. Zhang, A. F. Anghel, M. D. Iredell, S. Moorthi, and H.-M. Juang (2008), Tidal variability in the lower thermosphere: Comparison of Whole Atmosphere Model (WAM) simulations with observations from TIMED, *Geophys. Res. Lett.*, *35*, L03810, doi:10.1029/2007GL032584.

Alexander, S. P., and M. G. Shepherd (2010), Planetary wave activity in the polar lower stratosphere, *Atmos. Chem. Phys.*, *10*, 707–718, doi:10.5194/acp-10-707-2010.

Andrews, D. G., J. R. Holton, and C. B. Leovy (1987), *Middle Atmosphere Dynamics*, Academic Press, San Diego.

Angelats i Coll, M., and J. M. Forbes (2002), Nonlinear interactions in the upper atmosphere: The s = 1 and s = 3 nonmigrating semidiurnal tides, *J. Geophys. Res.*, *107*(A8), 1157, doi:10.1029/2001JA900179.

Avery, S. K., R. A. Vincent, A. Phillips, A. H. Manson, and G. J. Fraser (1989), High-latitude tidal behavior in the mesosphere and lower thermosphere, *J. Atmos. Terr. Phys.*, *51*, 595–608, doi:10.1016/0021-9169(89)90057-3.

Azeem, S. M. I., and G. G. Sivjee (2009), Multiyear observations of tidal oscillations in OH M(3,1) rotational temperatures at South Pole, Antarctica, *J. Geophys. Res.*, *114*, A06312, doi:10.1029/2008JA013976.

Baumgaertner, A. J. G., A. J. McDonald, G. J. Fraser, and G. E. Plank (2005), Long-term observations of mean winds and tides in the upper mesosphere and lower thermosphere above Scott Base, Antarctica, *J. Atmos. Sol. Terr. Phys.*, *67*, 1480–1496, doi:10.1016/j.jastp.2005.07.018.

Baumgaertner, A. J. G., M. J. Jarvis, A. J. McDonald, and G. J. Fraser (2006), Observations of the wavenumber 1 and 2 components of the semidiurnal tide over Antarctica, *J. Atmos. Sol. Terr. Phys.*, *68*, 1195–1214.

Chen, C., X. Chu, A. J. McDonald, S. L. Vadas, Z. Yu, W. Fong, and X. Lu (2013), Inertia-gravity waves in Antarctica: A case study using simultaneous lidar and radar measurements at McMurdo/Scott Base (77.8°S, 166.7°E), *J. Geophys. Res. Atmos.*, *118*, 2794–2808, doi:10.1002/jgrd.50318.

Chu, X., G. Papen, W. Pan, C. S. Gardner, and J. Gelbwachs (2002), Fe Boltzmann temperature lidar: Design, error analysis, and first results from the North and South poles, *Appl. Opt.*, *41*, 4400–4410.
Chu, X., W. Huang, W. Fong, Z. Yu, Z. Wang, J. A. Smith, and C. S. Gardner (2011a), First lidar observations of polar mesospheric clouds and Fe temperatures at McMurdo (77.8°S, 166.7°E), Antarctica, *Geophys. Res. Lett.*, *38*, L16810, doi:10.1029/2011GL048373.
Chu, X., Z. Yu, C. S. Gardner, C. Chen, and W. Fong (2011b), Lidar observations of neutral Fe layers and fast gravity waves in the thermosphere (110–155 km) at McMurdo (77.8°S, 166.7°E), Antarctica, *Geophys. Res. Lett.*, *38*, L23807, doi:10.1029/2011GL050016.
Espy, P. J., G. O. L. Jones, G. R. Swenson, J. Tang, and M. J. Taylor (2004), Seasonal variations of the gravity wave momentum flux in the Antarctic mesosphere and lower thermosphere, *J. Geophys. Res.*, *109*, D23109, doi:10.1029/2003JD004446.
Fesen, C. G. (1997), Geomagnetic activity effects on thermospheric tides: A compendium of theoretical predictions, *J. Atmos. Sol. Terr. Phys.*, *59*, 785–803.
Fesen, C. G., R. G. Roble, and E. C. Ridley (1991), Thermospheric tides at equinox: Simulations with coupled composition and auroral forcings: 1. Diurnal component, *J. Geophys. Res.*, *96*, 3647–3661.
Fesen, C. G., A. D. Richmond, and R. G. Roble (1993), Theoretical effects of geomagnetic activity on thermospheric tides, *J. Geophys. Res.*, *98*(A9), 15,599–15,612, doi:10.1029/93JA01188.
Forbes, J. M., and D. Wu (2006), Solar tides as revealed by measurements of mesosphere temperature by the MLS experiment on UARS, *J. Atmos. Sci.*, *63*, 1776–1797.
Forbes, J. M., N. A. Makarov, and Y. I. Portnyagin (1995), First results from meteor radar at South Pole: A large 12 hour oscillation with zonal wave number one, *Geophys. Res. Lett.*, *22*, 3247–3250, doi:10.1029/95GL03370.
Forbes, J. M., S. E. Palo, and X. Zhang (2000), Variability of the ionosphere, *J. Atmos. Sol. Terr. Phys.*, *62*, 685–693.
Forbes, J. M., X. Zhang, S. Palo, J. Russell, C. J. Mertens, and M. Mlynczak (2008), Tidal variability in the ionospheric dynamo region, *J. Geophys. Res.*, *113*, A02310, doi:10.1029/2007JA012737.
Fritts, D. C., and R. A. Vincent (1987), Mesospheric momentum flux studies at Adelaide, Australia: Observations and a gravity wave-tidal interaction model, *J. Atmos. Sci.*, *44*, 605–619.
Fuller-Rowell, T. J., D. Rees, and H. F. Parish (1991), Lower thermosphere coupling study: Comparison of observations with predictions of the University College London-Sheffield thermosphere-ionosphere model, *J. Geophys. Res.*, *96*, 1181–1202.
Fuller-Rowell, T. J., et al. (2008), Impact of terrestrial weather on the upper atmosphere, *Geophys. Res. Lett.*, *35*, L09808, doi:10.1029/2007GL032911.
Fuller-Rowell, T., F. Wu, R. Akmaev, T.-W. Fang, and E. Araujo-Pradere (2010), A whole atmosphere model simulation of the impact of a sudden stratospheric warming on thermosphere dynamics and electrodynamics, *J. Geophys. Res.*, *115*, A00G08, doi:10.1029/2010JA015524.
Fuller-Rowell, T., H. Wang, R. Akmaev, F. Wu, T.-W. Fang, M. Iredell, and A. Richmond (2011), Forecasting the dynamic and electrodynamic response to the January 2009 sudden stratospheric warming, *Geophys. Res. Lett.*, *38*, L13102, doi:10.1029/2011GL047732.
Gelbwachs, J. A. (1994), Iron Boltzmann factor LIDAR: Proposed new remote-sensing technique for mesospheric temperature, *Appl. Opt.*, *33*, 7151–7156.
Hagan, M. E., and J. M. Forbes (2002), Migrating and nonmigrating tides in the middle and upper atmosphere excited by tropospheric latent heat release, *J. Geophys. Res.*, *107*(D24), 4754, doi:10.1029/2001JD001236.
Hagan, M. E., and R. G. Roble (2001), Modeling diurnal tidal variability with the National Center for Atmospheric Research thermosphere-ionosphere-mesosphere-electrodynamics general circulation model, *J. Geophys. Res.*, *106*(A11), 24,869–24,882.
Hauchecorne, A., and M. Chanin (1980), Density and temperature profiles obtained by lidar between 35 and 70 km, *Geophys. Res. Lett.*, *7*(8), 565–568, doi:10.1029/GL007i008p00565.
Hecht, J. H., R. L. Walterscheid, D. C. Firtts, J. R. Isler, D. C. Senft, C. S. Gardner, and S. J. Franke (1997), Wave breaking signatures in OH airglow and sodium densities and temperature: 1. Airglow imaging, Na lidar, and MF radar observations, *J. Geophys. Res.*, *102*, 6655–6668.
Hernandez, G., G. J. Fraser, and R. W. Smith (1993), Mesospheric 12 hour oscillation near South Pole, Antarctica, *Geophys. Res. Lett.*, *20*, 1787–1790.
Hibbins, R. E., O. J. Marsh, A. J. McDonald, and M. J. Jarvis (2010), Interannual variability of the S = 1 and S = 2 components of the semidiurnal tide in the Antarctic MLT, *J. Atmos. Sol. Terr. Phys.*, *72*, 794–800, doi:10.1016/j.jastp.2010.03.026.
Immel, T. J., E. Sagawa, S. L. England, S. B. Henderson, M. E. Hagan, S. B. Mende, H. U. Frey, C. M. Swenson, and L. J. Paxton (2006), Control of equatorial ionospheric morphology by atmospheric tides, *Geophys. Res. Lett.*, *33*, L15108, doi:10.1029/2006GL026161.
Liu, A. Z., R. G. Roble, J. H. Hecht, M. F. Larsen, and C. S. Gardner (2004), Unstable layers in the mesopause region observed with Na lidar during the Turbulent Oxygen Mixing Experiment (TOMEX) campaign, *J. Geophys. Res.*, *109*, D02S02, doi:10.1029/2002JD003056.
Liu, A. Z., X. Lu, and S. J. Franke (2013), Diurnal variation of gravity wave momentum flux and its forcing on the diurnal tide, *J. Geophys. Res. Atmos.*, *118*, 1668–1678, doi:10.1029/2012JD018653.
Lu, X., A. Z. Liu, G. R. Swenson, T. Li, T. Leblanc, and I. S. McDermid (2009), Gravity wave propagation and dissipation from the stratosphere to the lower thermosphere, *J. Geophys. Res.*, *114*, D11101, doi:10.1029/2008JD010112.
Lu, X., A. Z. Liu, J. Oberheide, Q. Wu, T. Li, Z. Li, G. R. Swenson, and S. J. Franke (2011), Seasonal variability of the diurnal tide in the mesosphere and lower thermosphere over Maui, Hawaii (20.7°N, 156.3°W), *J. Geophys. Res.*, *116*, D17103, doi:10.1029/2011JD015599.
Lu, X., X. Chu, T. Fuller-Rowell, L. Chang, W. Fong, and Z. Yu (2013), Eastward propagating planetary waves with periods of 1–5 days in the winter Antarctic stratosphere as revealed by MERRA and lidar, *J. Geophys. Res. Atmos.*, *118*, 9565–9578, doi:10.1002/jgrd.50717.
Lübken, F.-J., J. Höffner, T. P. Viehl, B. Kaifler, and R. J. Morris (2011), First measurements of thermal tides in the summer mesopause region at Antarctic latitudes, *Geophys. Res. Lett.*, *38*, L24806, doi:10.1029/2011GL050045.
McDonald, A. J., R. E. Hibbins, and M. J. Jarvis (2011), Properties of the quasi 16 day wave derived from EOS MLS observations, *J. Geophys. Res.*, *116*, D06112, doi:10.1029/2010JD014719.
Mlynczak, M. G., and S. Solomon (1993), A detailed evaluation of the heating efficiency in the middle atmosphere, *J. Geophys. Res.*, *98*, 10,517–10,541.
Müller-Wodarg, I. C. F., A. D. Aylward, and T. J. Fuller-Rowell (2001), Tidal oscillations in the thermosphere: A theoretical investigation of their sources, *J. Atmos. Sol. Terr. Phys.*, *63*, 899–914.
Murphy, D. J., M. Tsutsumi, D. M. Riggin, G. O. L. Jones, R. A. Vincent, M. E. Hagan, and S. K. Avery (2003), Observations of a nonmigrating component of the semidiurnal tide over Antarctica, *J. Geophys. Res.*, *108*(D8), 4241, doi:10.1029/2002JD003077.
Murphy, D. J., et al. (2006), A climatology of tides in the Antarctic mesosphere and lower thermosphere, *J. Geophys. Res.*, *111*, D23104, doi:10.1029/2005JD006803.
Murphy, D. J., T. Aso, D. C. Fritts, R. E. Hibbins, A. J. McDonald, D. M. Riggin, M. Tsutsumi, and R. A. Vincent (2009), Source regions for Antarctic MLT nonmigrating semidiurnal tides, *Geophys. Res. Lett.*, *36*, L09805, doi:10.1029/2008GL037064.
Oberheide, J., Q. Wu, T. L. Killeen, M. E. Hagan, and R. G. Roble (2006), Diurnal nonmigrating tides from TIMED Doppler Interferometer wind data: Monthly climatologies and seasonal variations, *J. Geophys. Res.*, *111*, A10S03, doi:10.1029/2005JA011491.

Picone, J. M., A. E. Hedin, D. P. Drob, and A. C. Aikin (2002), NRLMSISE-00 empirical model of the atmosphere: Statistical comparisons and scientific issues, *J. Geophys. Res.*, *107*(A12), 1468, doi:10.1029/2002JA009430.

Portnyagin, Y., J. Forbes, E. Merzlyakov, N. Makarov, and S. Palo (1998), The summertime 12-h wind oscillation with zonal wave number s = 1 in the lower thermosphere over the South Pole, *Ann. Geophys.*, *16*, 828–837.

Randel, W. J. (1988), The seasonal evolution of planetary waves in the southern hemisphere stratosphere and troposphere, *Q. J. R. Meteorol. Soc.*, *114*, 1385–1409, doi:10.1002/qj.49711448403.

Rishbeth, H., and O. K. Garriott (1969), *Introduction to Ionospheric Physics*, Academic Press, New York.

Russell, J. M., M. G. Mlynczak, L. L. Gordley, J. J. Tansock, and R. W. Esplin (1999), Overview of the SABER experiment and preliminary calibration results, *Proc. SPIE Int. Soc. Opt. Eng.*, *3756*, 277–288, doi:10.1117/12.366382.

Smith, A. K. (2004), Physics and chemistry of the mesopause region, *J. Atmos. Sol. Terr. Phys.*, *66*, 839–857.

Smith, A. K., D. R. Marsh, and A. C. Szymczak (2003), Interaction of chemical heating and the diurnal tide in the mesosphere, *J. Geophys. Res.*, *108*(D5), 4164, doi:10.1029/2002JD002664.

Smith, A. K., D. V. Pancheva, N. J. Mitchell, D. R. Marsh, J. M. Russell III, and M. G. Mlynczak (2007), A link between variability of the semidiurnal tide and planetary waves in the opposite hemisphere, *Geophys. Res. Lett.*, *34*, L07809, doi:10.1029/2006GL028929.

Taylor, R. J. (1997), *An Introduction to Error Analysis*, 2nd ed., Univ. Science Books, Sausalito, Calif.

Walterscheid, R. L. (1981), Inertio-gravity wave induced accelerations of mean flow having an imposed periodic component: Implications for tidal oscillations in the meteor region, *J. Geophys. Res.*, *86*, 9698–9706.

Wang, H., T. J. Fuller-Rowell, R. A. Akmaev, M. Hu, D. T. Kleist, and M. D. Iredell (2011), First simulations with a whole atmosphere data assimilation and forecast system: The January 2009 major sudden stratospheric warming, *J. Geophys. Res.*, *116*, A12321, doi:10.1029/2011JA017081.

Wang, Z., X. Chu, W. Huang, W. Fong, J. A. Smith, and B. Roberts (2012), Refurbishment and upgrade of Fe Boltzmann/Rayleigh temperature lidar at Boulder for a McMurdo lidar campaign in Antarctica, *Proceedings of the 26th International Laser Radar Conference*, pp. 207-210, Porto Heli, Greece, 25–29 June 2012.

Weimer, D. R. (2005), Improved ionospheric electrodynamic models and application to calculating Joule heating rates, *J. Geophys. Res.*, *110*, A05306, doi:10.1029/2004JA010884.

Yamashita, K., S. Miyahara, Y. Miyoshi, K. Kawano, and J. Ninomiya (2002), Seasonal variation of non-migrating semidiurnal tide in the polar MLT region in a general circulation model, *J. Atmos. Sol. Terr. Phys.*, *64*, 1083–1094.

Zhang, X., J. M. Forbes, and M. E. Hagan (2010a), Longitudinal variation of tides in the MLT region: 1. Tides driven by tropospheric net radiative heating, *J. Geophys. Res.*, *115*, A06316, doi:10.1029/2009JA014897.

Zhang, X., J. M. Forbes, and M. E. Hagan (2010b), Longitudinal variation of tides in the MLT region: 2. Relative effects of solar radiative and latent heating, *J. Geophys. Res.*, *115*, A06317, doi:10.1029/2009JA014898.